

Local imaging of diamagnetism in proximity-coupled niobium nanoisland arrays on gold thin films

Logan Bishop-Van Horn^{1,2,*}, Irene P. Zhang^{2,3,*}, Emily N. Waite⁴, Ian Mondragon-Shem^{5,6}, Scott Jensen⁴, Junseok Oh⁴, Tom Lippman¹, Malcolm Durkin⁷, Taylor L. Hughes⁴, Nadya Mason⁴, Kathryn A. Moler^{2,3}, and Ilya Sochnikov^{4,8,9,†}

¹Department of Physics, Stanford University, Stanford, California 94305, USA

²Stanford Institute for Materials and Energy Sciences, SLAC National Accelerator Laboratory, Menlo Park, California 94025, USA

³Department of Applied Physics, Stanford University, Stanford, California 94305, USA

⁴Department of Physics and Materials Research Laboratory, University of Illinois, Urbana, Illinois 61801, USA

⁵Department of Physics and Astronomy, Northwestern University, Evanston, Illinois 60208, USA

⁶Materials Science Division, Argonne National Laboratory, Argonne, Illinois 60439, USA

⁷Department of Physics, University of Colorado Boulder, Boulder, Colorado 80305, USA

⁸Department of Physics, University of Connecticut, Storrs, Connecticut 06269, USA

⁹Institute of Material Science, University of Connecticut, Storrs, Connecticut 06269, USA



(Received 17 May 2022; revised 28 July 2022; accepted 16 August 2022; published 30 August 2022)

In this work, we study the effect of engineered disorder on the local magnetic response of proximity-coupled superconducting island arrays by comparing scanning superconducting quantum interference device (SQUID) susceptibility measurements to a model in which we treat the system as a network of one-dimensional (1D) superconductor–normal-metal–superconductor Josephson junctions, each with a Josephson coupling energy E_J determined by the junction length or distance between islands. We find that the disordered arrays exhibit a spatially inhomogeneous diamagnetic response which, for low local applied magnetic fields, is well described by this junction network model, and we discuss these results as they relate to inhomogeneous 2D superconductors. Our model of the static magnetic response of the arrays does not fully capture the onset of nonlinearity and dissipation with increasing applied field, as these effects are associated with vortex motion due to the dynamic nature of the scanning SQUID susceptometry measurement. This work demonstrates a model 2D superconducting system with engineered disorder, and it highlights the impact of dissipation on the local magnetic properties of 2D superconductors and Josephson junction arrays.

DOI: [10.1103/PhysRevB.106.054521](https://doi.org/10.1103/PhysRevB.106.054521)

I. INTRODUCTION

The effects of disorder and inhomogeneity on the superconducting properties of thin films have attracted both practical and theoretical interest, particularly in the presence of spatial correlations [1–3]. Disorder has been shown to weaken superconductivity in single-crystal Sr_2RuO_4 and thin-film $\text{YBa}_2\text{Cu}_2\text{O}_{7-\delta}$ [4,5]. In contrast, disorder in monolayers of TaS_2 was recently reported to enhance the critical transition temperature [6]. In single atomic layers of lead on silicon, the presence of disorder can lead to atomically short Josephson weak links [7]. The addition of correlated disorder in superconductors can be beneficial for some aspects of superconductivity compared to systems without correlation [8]. In $\text{YBa}_2\text{Cu}_2\text{O}_{7-\delta}$, microstructures of columnar defects introduced by irradiation pin flux lines more strongly than random point defects, shifting the irreversibility line significantly upward [9–11]. In two-dimensional (2D) superconductor-to-insulator systems, the existence of disorder is thought to create weakly coupled islands of superconductivity; with increasing disorder, such islands can

remain even beyond the superconductor-insulator transition [12,13]. In numerical studies of the quantum XY model, correlated disorder was shown to cause a broadening of the Berezinskii-Kosterlitz-Thouless (BKT) transition with respect to temperature, whereas uncorrelated disorder had no effect on the sharpness of the transition [14]. Inhomogeneity at any lengthscale can also complicate the interpretation of bulk or sample-averaged measurements.

Given the effect of both correlated and uncorrelated disorder on superconducting systems, one open question is as follows: How do spatial correlations in disorder affect the magnetic response of a 2D superconducting system? To explore this question, we used scanning superconducting quantum interference device microscopy (scanning SQUID microscopy or SSM) to measure the local diamagnetic response of arrays of niobium islands with proximity coupling via a thin layer of gold. Superconducting island arrays on normal metal can be a useful model for studying disorder in 2D superconductors, as both the disorder and the critical current can be engineered by changing the spacing between superconducting islands [15–17].

Previously, Eley *et al.* showed that transport in ordered arrays of niobium islands on gold can be modeled by treating the entire array as a single diffusive superconductor–normal-metal–superconductor (SNS) junction with a junction length

*These authors contributed equally to this work.

†ilya.sochnikov@uconn.edu

equal to the island-to-island spacing, d [18]. Neighboring islands couple to each other by proximitizing the underlying gold, and the system undergoes a BKT transition with decreasing temperature [19–21]. In this work, we study the effect of engineered disorder on the local magnetic response of proximity-coupled superconducting island arrays by comparing SSM susceptibility measurements to a model in which we treat the system as a network of one-dimensional (1D) SNS Josephson junctions, each with a Josephson coupling energy E_J determined by the junction length or distance between islands. We find that the disordered arrays exhibit a spatially inhomogeneous diamagnetic response that, for low applied magnetic fields, is well described by this junction network model. Upon increasing the applied field, the response becomes nonlinear and dissipative, with both the degree of nonlinearity and the spatial structure of the dissipative effects depending strongly on the details of the engineered disorder in a way that is not fully captured by the model.

II. METHODS

We measured arrays with three types of island configurations: (i) ordered, (ii) uncorrelated disorder, and (iii) correlated disorder (Fig. 1). The ordered array consists of a $100 \times 100 \mu\text{m}^2$ square lattice of nominally circular niobium islands, with a lattice constant $a = 500 \text{ nm}$; each island in the array has a diameter $D_{\text{island}} = 260 \text{ nm}$ and a height of 100 nm. The minimum edge-to-edge island spacing in the ordered array is therefore $d_0 = a - D_{\text{island}} = 240 \text{ nm}$. The disordered arrays were generated by displacing the island positions in the ordered array by a distance $|\Delta \mathbf{R}|$ drawn from a normal distribution $f(|\Delta \mathbf{R}|) = \frac{1}{\sigma \sqrt{2\pi}} \exp(-\frac{|\Delta \mathbf{R}|^2}{2\sigma^2})$ with standard deviation σ [22]. For arrays with uncorrelated disorder, this process defined the final island locations. To generate correlated disorder, an additional filter kernel was applied to normally distributed island displacements so that the covariance of the displacements of any two islands is described by the correlation function

$$R(z) = \sigma^2 \exp\left(-\frac{z^2}{\ell^2}\right), \quad (1)$$

where z is the center-to-center distance between pairs of islands in the square lattice, and $\ell = 5 \mu\text{m}$ is the correlation length [22].

For each array, the locations of the islands were patterned onto a 10-nm-thick gold film with lateral dimensions $80 \times 80 \mu\text{m}^2$ using electron beam lithography, after which the niobium islands were deposited using electron beam evaporation. Transport measurements performed in a dilution refrigerator with a base temperature of 10 mK show two distinct transition temperatures: one from the niobium islands themselves entering the superconducting regime (T_1), and a second, lower transition temperature (T_2) marking the onset of phase coherence in the proximitized gold film [16] (see the Supplemental Material [23], which includes Refs. [24–30]). The superconducting transition temperature of the niobium islands themselves is lower than that of bulk niobium, consistent with previous work [31].

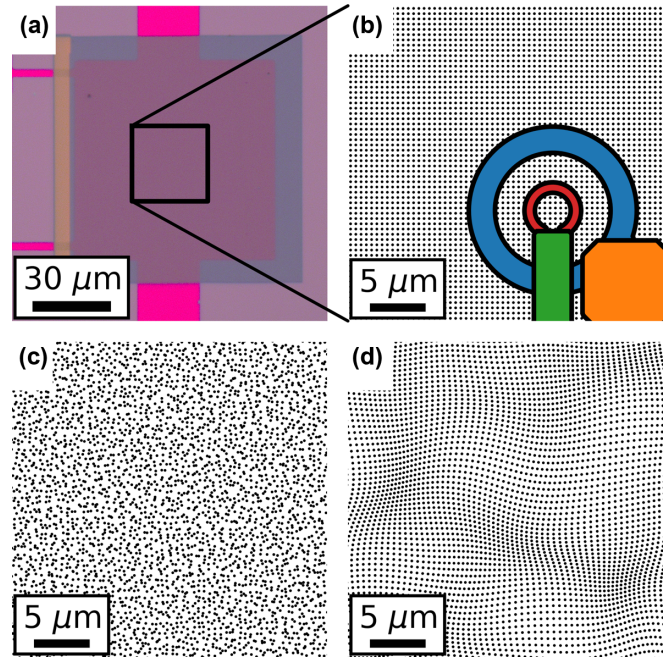


FIG. 1. Device and sensor geometry. (a) Optical image of the ordered array. The background is the SiO₂ substrate, the bright pink regions are bare gold film, the gray region is niobium islands directly on SiO₂, and the dark pink central $80 \mu\text{m} \times 80 \mu\text{m}$ region is niobium islands on top of the gold film. (b)–(d) Schematic of the designed island positions for a $30 \mu\text{m} \times 30 \mu\text{m}$ region of (b) the ordered array, (c) an uncorrelated disordered array ($\sigma = 40\%$), and (d) a correlated disordered array ($\sigma = 15\%$). The islands are drawn to scale, i.e., each island has a diameter of 260 nm. The SQUID susceptometer geometry is shown in (b), with the field coil in blue (large radius) and the pickup loop in red (small radius). There are also superconducting shields covering the field coil and pickup loop leads, which are shown as orange and green polygons, respectively.

The arrays were studied using a scanning SQUID microscope mounted in a helium-3 refrigerator at its base temperature, $T = 400 \text{ mK}$. The scanning SQUID susceptometer used in this work consists of gradiometric concentric pickup loop and field coil pairs, with pickup loop inner radius $r_{\text{PL}}^{\text{inner}} = 1.7 \mu\text{m}$ (outer radius $r_{\text{PL}}^{\text{outer}} = 2.7 \mu\text{m}$) and field coil inner radius $r_{\text{FC}}^{\text{inner}} = 5.5 \mu\text{m}$ (outer radius $r_{\text{FC}}^{\text{outer}} = 8.0 \mu\text{m}$) [Fig. 1(b)] [32]. Using an SR830 lock-in amplifier, we apply a local low-frequency ac magnetic field to the array using the field coil carrying current I_{FC} , and we record the flux Φ_{PL} through the pickup loop generated by the array's response as a function of the field coil position. We define this response, normalized by the current through the field coil, as the local susceptibility, $\phi = \Phi_{\text{PL}}/I_{\text{FC}}$, which we report in units of Φ_0/A , where Φ_0 is the superconducting flux quantum. The gradiometric design of the SQUID susceptometer allows us to detect a local magnetic response due to current flowing in the arrays, $\Phi_{\text{PL}} = \phi I_{\text{FC}}$, which is much smaller than the flux through the pickup loop due to the field coil. For example, the measurements presented below have a typical signal magnitude of $\sim 1 \Phi_0/A$ (with signal-to-noise ratio $\gg 1$ except at very small I_{FC}), which is approximately 1/1000 of the intrinsic mutual inductance between the field coil and the

TABLE I. Designed disorder in measured arrays. The standard deviation σ of the island displacement distribution is expressed as a percentage of the island spacing in the ordered array. The island positions in UC4 are generated without reference to the ordered array. Instead, we randomly select points in a $100 \times 100 \mu\text{m}^2$ area according to a uniform distribution.

Sample	Type of disorder	σ
Ordered	Ordered	0%
UC3	Uncorrelated	40%
UC4	Uncorrelated	Uniformly distributed
C2	Correlated	10%
C3	Correlated	15%

pickup loop. (See the Supplemental Material [23] for a more detailed description of the sensor design and susceptometry measurement technique.) The susceptibility ϕ has a component ϕ' that is in-phase with the applied field and a component ϕ'' that is out-of-phase with the applied field. The in-phase component is a measure of the local diamagnetic screening in a superconducting sample and hence the London penetration depth or superfluid density, while the out-of-phase component is a measure of dissipative currents. The measurements were performed at nominally zero applied global field, so that the

only applied field was the local ac field from the susceptometer field coil.

III. RESULTS AND DISCUSSION

We imaged five arrays: one completely ordered, two with uncorrelated disorder, and two with correlated disorder, as summarized in Table I. We applied root-mean-square (rms) field coil currents I_{FC} from 0.012 mA up to 3.024 mA, corresponding to about 1–300 μT at the center of the field coil, at a frequency of $f_{\text{FC}} = 800$ Hz to probe the linear and nonlinear regimes of the diamagnetic response. The in-phase susceptibility images reveal striking differences in the spatial structure of the diamagnetic susceptibility between the completely ordered array and arrays with disorder (Fig. 2). At the lowest field coil current, the ordered array shows homogeneous diamagnetic screening [Fig. 2(a)]. From the magnitude of the in-phase susceptibility signal, we estimate an effective 2D penetration depth (equal to half the Pearl length [33]) of $\Lambda > 500 \mu\text{m}$, indicating weak Meissner screening and a small superfluid density [34]. Only at higher field coil currents does spatial structure appear in the form of reduced diamagnetism at the edge of the array [Figs. 2(b) and 2(c)]. In contrast, in all the arrays with engineered disorder, our measurements reveal significant spatial inhomogeneity in the local diamagnetic response. The diamagnetism in these arrays

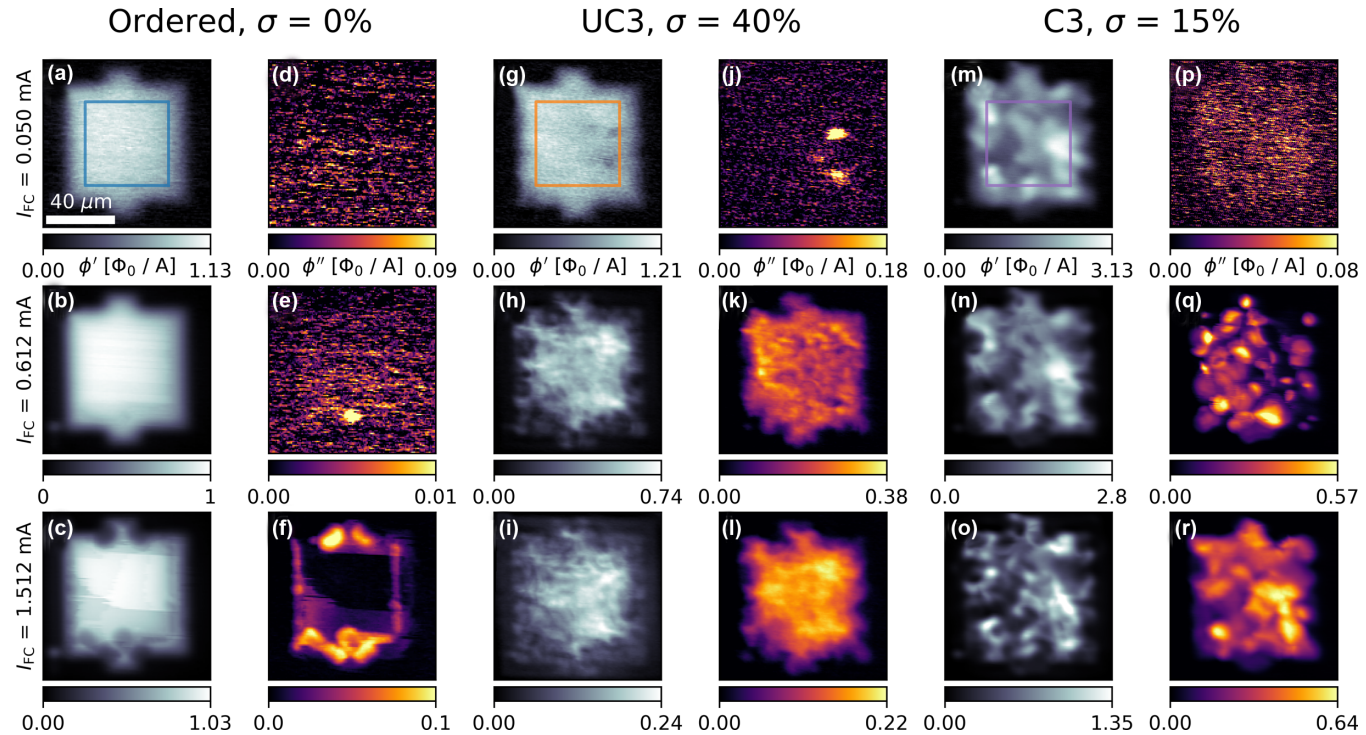


FIG. 2. Inhomogeneous, nonlinear diamagnetic response in disordered arrays under increasing local applied field. In-phase susceptibility ϕ' (black-to-white colormap) and out-of-phase susceptibility ϕ'' (black-to-yellow colormap) for the three arrays whose island positions are shown in Figs. 1(b)–1(d), measured at three different rms field coil currents I_{FC} . All images share the scale bar given in panel (a) and were taken at the same nominal sensor height and temperature. Note that panels (d,e,j,p) only show noise, as ϕ'' was below the measurement noise floor for these measurements with small I_{FC} . The colored boxes in panels (a,g,m) indicate the central $50 \times 50 \mu\text{m}^2$ regions for which the distributions of ϕ' are shown as a function of I_{FC} in Figs. 3(a), 3(b) and 3(e), respectively. Measurements of all five samples listed in Table I can be found in the Supplemental Material [23].

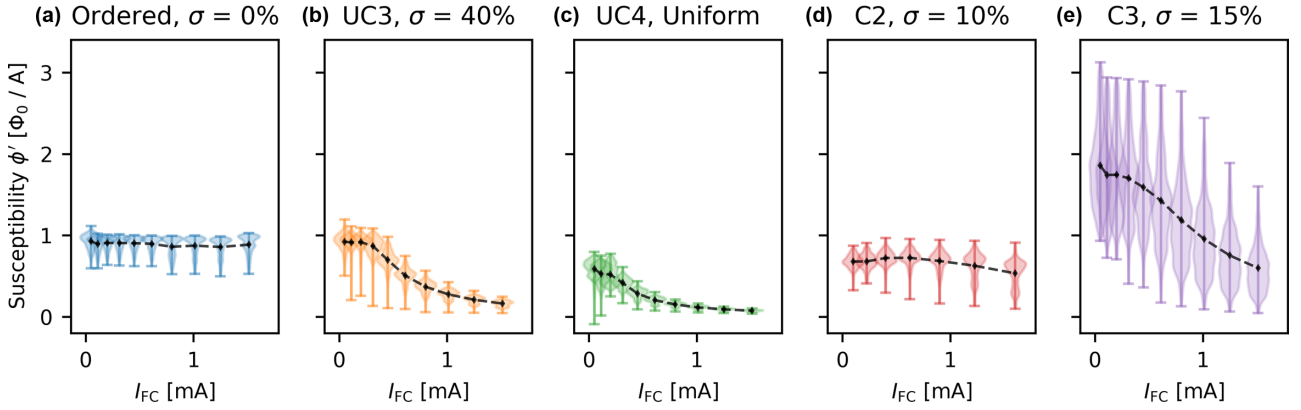


FIG. 3. Distribution of in-phase susceptibility ϕ' in SSM images for all measured samples as a function of field coil current. The shaded “violins” show the empirical probability distribution of the susceptibility signal ϕ' in the central $50 \times 50 \mu\text{m}^2$ region of each array [see the colored boxes in Figs. 2(a), 2(g) and 2(m)], and the black diamonds and dashed lines show the average over this region. The response of the ordered array (a) is linear in the sense that the magnitude and spatial distribution of the diamagnetic susceptibility are constant as a function of the applied field. In contrast, the disordered arrays (b)–(e) respond nonlinearly at all but the lowest field coil currents. The magnitude of ϕ' depends strongly on the sensor height, or the distance between the SQUID field coil and the sample. The data for C2 were taken at 2–3 μm higher sensor height compared to the ordered and uncorrelated arrays, resulting in a relative overall reduction in signal magnitude. Similarly, the stronger average in-phase susceptibility for C3 most likely indicates that this sample was measured with a smaller sensor height than the ordered and uncorrelated arrays [23].

varies on a lengthscale of a few microns over the entirety of the array [Figs. 2(g)–2(i) and 2(m)–2(o)]. In arrays with correlated disorder, this inhomogeneity can be seen even at the smallest applied field [Fig. 2(m)].

The magnitude and spatial structure of the diamagnetic susceptibility are not constant as a function of the applied field. In Fig. 3, the distribution of in-phase diamagnetic susceptibility for each array is plotted as a function of applied field coil current, revealing differences between the ordered and disordered samples in the linearity of the diamagnetic response with respect to the local applied field. Because ϕ' necessarily goes to zero at the edges of the arrays, in Fig. 3 we plot the distribution of ϕ' only from the central $50 \times 50 \mu\text{m}^2$ region of each array [see the colored boxes in Figs. 2(a), 2(g) and 2(m)]. Except near the edges of the gold film, the ordered sample remains in the linear regime (i.e., the susceptibility is constant as a function of applied field, and the out-of-phase susceptibility ϕ'' is small) up to $I_{\text{FC}} = 1.512 \text{ mA}$ [Figs. 2(a)–2(f) and Fig. 3(a)], while the disordered samples enter the nonlinear regime, with decreasing in-phase susceptibility ϕ' and significant dissipative out-of-phase susceptibility ϕ'' , at applied field coil currents as low as $I_{\text{FC}} = 0.312 \text{ mA}$ [Figs. 2(g)–2(l) and 2(m)–2(r), and Figs. 3(b)–3(e)]. At the highest I_{FC} , the ordered array begins to exhibit an inhomogeneous response [Figs. 2(c) and 2(f)], which we attribute to heating of the gold film due to vortex motion near the edges of the array [23].

To explore the role of disorder in the inhomogeneous, nonlinear magnetic response of this engineered 2D superconductor, we have modeled the system as a network of 1D SNS Josephson junctions in which pairs of adjacent islands form junctions with critical current I_c , or Josephson energy $E_J = I_c \Phi_0 / 2\pi$, determined by the junction length or edge-to-edge island spacing d (see Fig. 4). Eley *et al.* found that for ordered triangular arrays of niobium nanoislands on gold, the dependence of the critical current of the entire array on

edge-to-edge island spacing d and temperature T is well described by the expression for a single diffusive SNS junction:

$$I_c(d, T) = c_0 \frac{E_{\text{Th}}(d)}{eR_N} \left[1 - c_1 \exp \left(-\frac{c_0 E_{\text{Th}}(d)}{3.2 k_B T} \right) \right], \quad (2)$$

where R_N is the normal state resistance, k_B is Boltzmann’s constant, and c_0 and c_1 are dimensionless fitting parameters, which are of order 1 [18,35]. The Thouless energy E_{Th} is given by $E_{\text{Th}}(d) = \hbar D / d^2$, where D is the normal-metal diffusion constant, with $D = 95 \text{ cm}^2/\text{s}$ for the gold films studied here. At temperatures T that are small compared to the Thouless energy E_{Th}/k_B ($\approx 1.26 \text{ K}$ for the ordered array), Eq. (2) is dominated by the term $c_0 E_{\text{Th}} / eR_N \propto 1/d^2$. We therefore assume that the critical current of each junction is given by $I_c(d) = I_0(d_0/d)^2$, where $d_0 = 240 \text{ nm}$ is the minimum island spacing for the ordered array [Fig. 1(b)] and I_0 is a constant that corresponds to the maximum critical current per junction in the ordered array. The value of I_0 determines the overall strength of the diamagnetic response, and we select it to roughly match the magnitude of the measured in-phase susceptibility.

We model the field coil and pickup loop as 1D circular loops with radii $r_{\text{FC}} = 6.8 \mu\text{m}$ and $r_{\text{PL}} = 2.5 \mu\text{m}$, respectively (see Fig. 4). Given the applied magnetic vector potential $\mathbf{A}(\mathbf{r})$ due to a current I_{FC} in the field coil, we solve for the superconducting phase φ_i of each island i centered at position \mathbf{r}_i in the network, subject to the constraints of current conservation and phase single-valuedness, via a large-scale nonlinear programming solver [23,36,37]. We then calculate the supercurrent flowing between each pair of islands (i, j) assuming a sinusoidal current-phase relation $I_{ij}(\theta_{ij}, d_{ij}) = I_c(d_{ij}) \sin \theta_{ij}$, where $d_{ij} = |\mathbf{r}_i - \mathbf{r}_j| - D_{\text{island}}$ is the junction length and $\theta_{ij} = \varphi_j - \varphi_i - 2\pi \Phi_0^{-1} \int_{\mathbf{r}_i}^{\mathbf{r}_j} \mathbf{A}(\mathbf{r}) \cdot d\mathbf{r}$ is the gauge-invariant phase across the junction. Finally, we compute the flux Φ_{PL} through

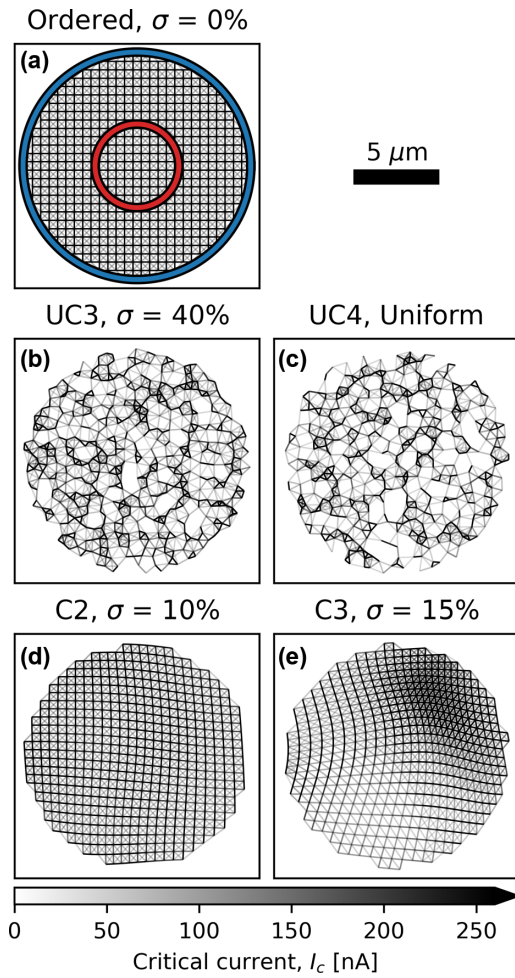


FIG. 4. Junction networks for a single field coil position for each of the five arrays studied in this work. Each line represents a single junction with critical current $I_c(d) = I_0(d_0/d)^2$ indicated by the shade of the line as shown by the colorbar. The colorbar is saturated at 260 nA because in the uncorrelated arrays there are a small number of very short (i.e., high critical current) junctions. Locations where lines intersect correspond to the center of a niobium island. For all five arrays, we use a junction cutoff radius $r_{\text{cutoff}} = 0.9 \mu\text{m}$ and a critical current scale of $I_0 = 260 \text{ nA}$. For the sake of visibility, the networks shown here use a patch radius $r_{\text{patch}} = r_{\text{FC}} = 6.8 \mu\text{m}$, which is a factor of 2.5 smaller than the patch radius used in the simulations. (a) The ordered array: a square lattice of islands with lattice constant $a = 500 \text{ nm}$. The blue circle shows the 1D loop used to model the field coil, and the red circle shows the 1D loop with radius $r_{\text{PL}} = 2.5 \mu\text{m}$ used to model the pickup loop. (b) Array UC3: uncorrelated disorder with $\sigma = 40\%$. (c) Array UC1: uniformly distributed island positions. (c) Array C2: correlated disorder with $\sigma = 10\%$. (d) Array C3: correlated disorder with $\sigma = 15\%$.

the pickup loop due to the supercurrent flowing in the network to obtain a simulated in-phase susceptibility $\phi' = \Phi_{\text{PL}}/I_{\text{FC}}$.

It is not computationally practical to model the response of all $\sim 25\,000$ islands in an array simultaneously, so we make two simplifying approximations. First, for each field coil position, we construct a network or graph containing only islands inside a “patch” of radius $r_{\text{patch}} = 17 \mu\text{m} = 2.5 \times r_{\text{FC}}$ around the center of the field coil. If the field coil is

positioned $z_{\text{FC}} = 2 \mu\text{m}$ above the array, the magnitude of the field from the field coil at the edge of the patch is $\approx 4\%$ of the field at the center, and junctions outside of the patch are at least $r_{\text{patch}} = 6.8 \times r_{\text{PL}}$ away from the center of the pickup loop. Therefore, junctions outside of r_{patch} are both weakly influenced by the field from the field coil and inefficient at coupling flux into the pickup loop, such that they do not contribute significantly to the susceptibility signal. In practice, increasing r_{patch} by 20%, from $2.5 \times r_{\text{FC}}$ to $3 \times r_{\text{FC}}$, increases the simulated susceptibility by $< 3\%$ and does not significantly affect the spatial structure [23]. Second, we assume that only islands whose centers lie within a radius $r_{\text{cutoff}} = 0.9 \mu\text{m}$ of one another form junctions. We chose $r_{\text{cutoff}} = 0.9 \mu\text{m}$ so that $2\xi_N < r_{\text{cutoff}} < 2a$, where $\xi_N = \sqrt{\hbar D/k_B T} \approx 0.425 \mu\text{m}$ is the normal-metal coherence length and $a = 0.5 \mu\text{m}$ is the ordered array lattice constant [18,38,39]. For this patch radius and junction cutoff radius, a typical patch contains a few thousand islands and 10 000-20 000 junctions [23]. Note that this model simulates the static magnetic response of the arrays, but the local field applied by the SQUID field coil varies sinusoidally at a frequency $f_{\text{FC}} = 800 \text{ Hz}$. Thus, an additional assumption is that f_{FC} is slow compared to other timescales in the system, such that the applied field can be approximated as time-independent. This model also neglects any inductive coupling between the junctions, which we expect to be small given the very weak screening in this system [40].

A comparison of the in-phase susceptibility ϕ' measured in the SSM experiments and simulated using the junction network model is shown in Fig. 5. The model reproduces the spatially uniform and linear magnetic response in the ordered array [Figs. 5(a), 5(f) and 5(k)]. In the arrays with uncorrelated disorder, the local diamagnetic response exhibits a granular spatial structure [Figs. 5(b) and 5(c)], and ϕ' is suppressed more rapidly with increasing applied field than in the ordered array or the arrays with correlated disorder [Figs. 3(b) and 3(c)]. Both of these effects are captured qualitatively by the junction network model [Figs. 5(g) and 5(h) and Figs. 5(l) and 5(m)]. The simulated susceptibility of the correlated arrays is in good agreement with the measurements [Figs. 5(d) and 5(i) and Figs. 5(e) and 5(j)], which is most easily visible in array C3 [Figs. 5(e) and 5(j)] as it exhibits the highest contrast and most distinctive spatial features in ϕ' as a function of field coil position.

The magnitude of ϕ' depends strongly on the distance z_{FC} between the field coil and the sample, and in this particular experiment there was significant uncertainty ($\sim 2\text{-}3 \mu\text{m}$) in z_{FC} . This is likely the cause of the discrepancy in the magnitude of ϕ' at low field coil currents between Fig. 3 (experiment) and Figs. 5(k)-5(o) (simulation), and it is why we plot the normalized susceptibility ϕ'/ϕ'_{max} in Figs. 5(a)-5(j). We expect that if z_{FC} were known with a high degree of certainty, the junction network model would reproduce quantitatively both the magnitude and spatial structure of the in-phase susceptibility at low applied fields.

Although susceptibility simulations using the junction network model do exhibit nonlinearity with increasing applied field as the gauge-invariant phase θ across junctions in the network becomes large enough that $\sin \theta \approx \theta$ is not a good approximation [see Figs. 5(k)-5(o) and the Supplemental Material [23]], in all cases the observed onset of nonlinearity

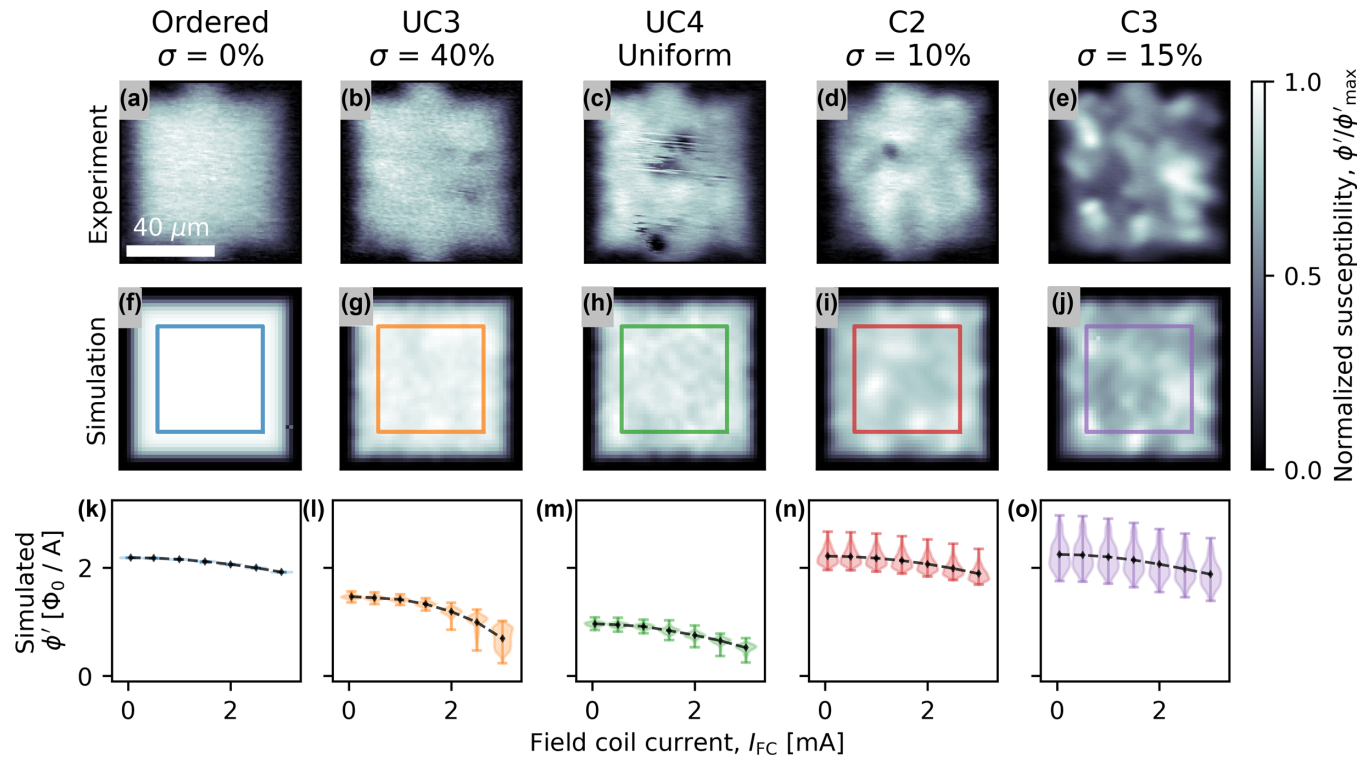


FIG. 5. Comparison between the measured and simulated in-phase susceptibility ϕ' for all five arrays. Top row (a)–(e): Normalized in-phase susceptibility ϕ'/ϕ'_{\max} measured at $I_{FC} = 0.05$ mA for panels (a,b,c,e) and $I_{FC} = 0.1$ mA for panel (d). Middle row (f)–(j): ϕ'/ϕ'_{\max} calculated using the junction network model with a field coil current of $I_{FC} = 0.05$ mA, a distance of $z_{FC} = 2$ μm between the sample surface and SQUID field coil, and a critical current scale of $I_0 = 260$ nA. Bottom row (k)–(o): Distribution of simulated in-phase susceptibility ϕ' vs field coil current, demonstrating the nonlinearity of the junction network model, the onset of which occurs at a higher field coil current than in experiment [compare to Fig. 3, where ϕ' is heavily suppressed in the uncorrelated arrays (b) and (c) well below $I_{FC} = 2$ mA]. As in Fig. 3, we plot only the distribution of ϕ' in the central $50 \times 50 \mu\text{m}^2$ region of each array [see the colored boxes in (f)–(j)]. The black diamonds and dashed lines indicate the average susceptibility in these regions. Note that there are several regions near the center of array UC4 [panel (c)] where niobium islands have been scraped off due to contact with the SQUID susceptometer, which is not accounted for in the model. See Fig. 4 and the Supplemental Material [23] for more details on the simulations.

in simulation occurs at a larger applied field than in experiment. For example, the ordered array shows appreciable out-of-phase response at $I_{FC} = 1.512$ mA [Fig. 2(f)], however the flux through an $a \times a = 500 \times 500 \text{ nm}^2$ square unit cell or ‘‘plaquette’’ due to a loop with radius $r_{FC} = 6.8 \mu\text{m}$ carrying $I_{FC} = 1.512$ mA is $<0.017 \Phi_0$, corresponding to a gauge-invariant phase difference of $\theta < 2\pi \times 0.017/4 \approx 0.027$ radians across each of the four junctions in the plaquette, a value for which $\sin \theta \approx \theta$ is a very good approximation. Furthermore, this mechanism for nonlinearity is purely geometric, having no dependence on the overall strength of the Josephson coupling in the system (which is set in the model by the critical current scale I_0).

This suggests that there is another mechanism contributing to the onset of nonlinearity and dissipation in these arrays. One candidate is motion of vortices induced in the 2D superconducting system above a lower critical field B_0^{crit} , as has been studied theoretically for uniform applied fields [41,42] and for nonuniform applied fields in the context of two-coil mutual inductance susceptibility measurements [43–45]. Lemberger and Ahmed [44] found that for a 2D superconductor in the weak screening (large Λ) limit with Ginzburg-Landau coherence length ξ subject to a nonuniform field from a point dipole or small current loop, there can

be no vortex-free state above a lower critical field $B_0^{\text{crit}} \approx \Phi_0/(2\rho_0\xi)$, where $\rho_0 \ll \Lambda$ is the radial distance from the magnetic source at which the applied field changes sign. This relationship between the coherence length ξ and the onset of vortex-related nonlinear magnetic response has been used to measure ξ in superconducting thin films [45]. For our field coil with radius $r_{FC} = 6.8 \mu\text{m}$ located 2 μm above the film, the applied field changes sign at $\rho_0 \approx 7.5 \mu\text{m}$. Assuming $\xi = a$ for the ordered square array with lattice constant a [39] gives a lower critical field $B_0^{\text{crit}} \approx 275 \mu\text{T}$, or a lower critical field coil current $I_{FC}^{\text{crit}} \approx 3.4$ mA. The actual applied field (or field coil current) at which nonlinearity due to vortex dynamics begins to occur is necessarily smaller than this maximum vortex-free field, which is consistent with the SQUID measurements [Fig. 2(f)]. In a homogeneous 2D superconductor, vortices are expected to first appear at the position with the highest superfluid momentum, i.e., the position where the vector potential $|\mathbf{A}(\mathbf{r})|$ is largest [44,46], and we expect the same to be true for the ordered array. Any vortices that are present will experience a force due to the local ac applied field from the field coil. If the vortices are not strongly pinned, they will move under this force, and it is this vortex motion that causes dissipation. For a detailed analysis of the impact of vortex dynamics on two-coil mutual inductance measure-

ments of 2D superconductors, see Ref. [47]. Viewed through this lens, our results (Figs. 2 and 3) suggest that disorder in the island spacing affects both the superfluid density and the coherence length ξ of the 2D superconductor formed by the proximity-coupled nanoislands, and that both quantities can be probed locally with SSM via the linear and nonlinear magnetic response, respectively.

Future work will focus on the magnetic response of ordered proximity-coupled island arrays as a function of the island spacing over a wider range of local applied ac field. Such measurements will allow us to validate our model for the island spacing dependence of the junction critical currents, $I_c(d)$, and quantify how well the junction network model describes nonlinearities at higher applied field, which will in turn inform the design of future experiments on arrays with different geometries and materials. Beyond scanning SQUID microscopy, the proximity effect model systems introduced here could potentially be studied with time- or frequency-resolved imaging to better understand the dynamics causing dissipative behavior [48].

In summary, we have demonstrated the design, control, and measurement of a model superconducting system with engineered disorder to simulate the spatial evolution of superfluid density and phase coherence in 2D superconductors with micron-scale disorder. Scanning SQUID microscopy measurements reveal a magnetic response that is nonlinear and spatially inhomogeneous, and this response can be tuned by changing the disorder landscape. For small applied fields, the local diamagnetic response of the arrays

is in good agreement with a model that treats the system as a network of Josephson junctions with island spacing-dependent Josephson coupling. However, we find that the onset of nonlinearity and dissipation with increasing applied field cannot be fully explained simply by considering the nonlinear (i.e., sinusoidal) current-phase relation of the junctions. This motivates future work on a theoretical description that incorporates the rich nonlinear and dissipative physics underlying this engineered, disordered 2D superconducting system.

ACKNOWLEDGMENTS

The fabrication of this project was carried out in part in the Material Research Laboratory Central Research Facilities, University of Illinois. Some of the computing for this project was performed on the Sherlock cluster. We would like to thank Stanford University and the Stanford Research Computing Center for providing computational resources and support that contributed to these research results. This work was primarily supported by the DOE “Quantum Sensing and Quantum Materials” Energy Frontier Research Center under Grant No. DE-SC0021238. Samples were fabricated with support from DOE Basic Energy Sciences under Grant No. DE-SC0012649. The SSM measurements were, in part, supported by the Gordon and Betty Moore Foundation, Grant No. GBMF3429 “Exotic Emergent Particles in Nanostructures.” Work at the University of Connecticut was supported by the State of Connecticut.

-
- [1] S. Alexander, Superconductivity of networks. A percolation approach to the effects of disorder, *Phys. Rev. B* **27**, 1541 (1983).
 - [2] M. N. Gastiasoro, F. Bernardini, and B. M. Andersen, Unconventional Disorder Effects in Correlated Superconductors, *Phys. Rev. Lett.* **117**, 257002 (2016).
 - [3] T. M. Lippman, B. Kalisky, H. Kim, M. A. Tanatar, S. L. Budko, P. C. Canfield, R. Prozorov, and K. A. Moler, Agreement between local and global measurements of the london penetration depth, *Physica C* **483**, 91 (2012).
 - [4] A. P. Mackenzie, R. K. W. Haselwimmer, A. W. Tyler, G. G. Lonzarich, Y. Mori, S. Nishizaki, and Y. Maeno, Extremely Strong Dependence of Superconductivity on Disorder in Sr_2RuO_4 , *Phys. Rev. Lett.* **80**, 161 (1998).
 - [5] J. Ye and K. Nakamura, Systematic study of the growth-temperature dependence of structural disorder and superconductivity in $\text{YBa}_2\text{Cu}_3\text{O}_{7-\delta}$ thin films, *Phys. Rev. B* **50**, 7099 (1994).
 - [6] J. Peng, Z. Yu, J. Wu, Y. Zhou, Y. Guo, Z. Li, J. Zhao, C. Wu, and Y. Xie, Disorder enhanced superconductivity toward TaS_2 monolayer, *ACS Nano* **12**, 9461 (2018).
 - [7] C. Brun, T. Cren, V. Cherkez, F. Debontridder, S. Pons, D. Fokin, M. C. Tringides, S. Bozhko, L. B. Ioffe, B. L. Altshuler, and D. Roditchev, Remarkable effects of disorder on superconductivity of single atomic layers of lead on silicon, *Nat. Phys.* **10**, 444 (2014).
 - [8] H. Alloul, J. Bobroff, M. Gabay, and P. J. Hirschfeld, Defects in correlated metals and superconductors, *Rev. Mod. Phys.* **81**, 45 (2009).
 - [9] L. Civale, A. D. Marwick, T. K. Worthington, M. A. Kirk, J. R. Thompson, L. Krusin-Elbaum, Y. Sun, J. R. Clem, and F. Holtzberg, Vortex Confinement by Columnar Defects in $\text{YBa}_2\text{Cu}_3\text{O}_7$ Crystals: Enhanced Pinning at High Fields and Temperatures, *Phys. Rev. Lett.* **67**, 648 (1991).
 - [10] D. R. Nelson and V. M. Vinokur, Boson Localization and Pinning by Correlated Disorder in High-Temperature Superconductors, *Phys. Rev. Lett.* **68**, 2398 (1992).
 - [11] Z. Tešanović and I. F. Herbut, High-field superconducting transition induced by correlated disorder, *Phys. Rev. B* **50**, 10389 (1994).
 - [12] Y. Dubi, Y. Meir, and Y. Avishai, Nature of the superconductor-insulator transition in disordered superconductors, *Nature (London)* **449**, 876 (2007).
 - [13] R. Crane, N. P. Armitage, A. Johansson, G. Sambandamurthy, D. Shahar, and G. Grüner, Survival of superconducting correlations across the two-dimensional superconductor-insulator transition: A finite-frequency study, *Phys. Rev. B* **75**, 184530 (2007).
 - [14] I. Maccari, L. Benfatto, and C. Castellani, Broadening of the Berezinskii-Kosterlitz-Thouless transition by correlated disorder, *Phys. Rev. B* **96**, 060508(R) (2017).
 - [15] B. Spivak and D. Khmel'nitskii, Influence of localization effects in a normal metal on the properties of SNS junction, *Pis'ma Zh. Eksp. Teor. Fiz.* **35**, 334 (1982) [*JETP Lett.* **35**, 412 (1982)].
 - [16] S. Eley, S. Gopalakrishnan, P. M. Goldbart, and N. Mason, Approaching zero-temperature metallic states in mesoscopic

- superconductor-normal-superconductor arrays, *Nat. Phys.* **8**, 59 (2012).
- [17] T. R. Naibert, H. Polshyn, R. Garrido-Menacho, M. Durkin, B. Wolin, V. Chua, I. Mondragon-Shem, T. Hughes, N. Mason, and R. Budakian, Imaging and controlling vortex dynamics in mesoscopic superconductor–normal-metal–superconductor arrays, *Phys. Rev. B* **103**, 224526 (2021).
- [18] S. Eley, S. Gopalakrishnan, P. M. Goldbart, and N. Mason, Dependence of global superconductivity on inter-island coupling in arrays of long SNS junctions, *J. Phys.: Condens. Matter* **25**, 445701 (2013).
- [19] V. L. Berezinskii, Destruction of long-range order in one-dimensional and two-dimensional systems possessing a continuous symmetry group. II. Quantum systems, *Zh. Eksp. Teor. Fiz.* **61**, 1144 (1971) [*Sov. Phys.—JETP* **34**, 610 (1972)].
- [20] J. M. Kosterlitz and D. J. Thouless, Ordering, metastability and phase transitions in two-dimensional systems, *J. Phys. C* **6**, 1181 (1973).
- [21] Z. Han, A. Allain, H. Arjmandi-Tash, K. Tikhonov, M. Feigel'man, B. Sacepe, and V. Bouchiat, Collapse of superconductivity in a hybrid tin-graphene josephson junction array, *Nat. Phys.* **10**, 380 (2014).
- [22] T. Lippman, Local measurements of the superconducting penetration depth, Ph.D. thesis, Stanford University, 2013.
- [23] See Supplemental Material at <http://link.aps.org/supplemental/10.1103/PhysRevB.106.054521> for SEM images of the niobium nanoislands, technical details related to scanning SQUID susceptometry, additional scanning SQUID data, transport data, and a more detailed description of the modeling.
- [24] B. W. Gardner, J. C. Wynn, P. G. Björnsson, E. W. J. Straver, K. A. Moler, J. R. Kirtley, and M. B. Ketchen, Scanning superconducting quantum interference device susceptometry, *Rev. Sci. Instrum.* **72**, 2361 (2001).
- [25] J. R. Kirtley, L. Paulius, A. J. Rosenberg, J. C. Palmstrom, C. M. Holland, E. M. Spanton, D. Schiessl, C. L. Jermain, J. Gibbons, Y.-K.-K. Fung, M. E. Huber, D. C. Ralph, M. B. Ketchen, G. W. Gibson, and K. A. Moler, Scanning SQUID susceptometers with sub-micron spatial resolution, *Rev. Sci. Instrum.* **87**, 093702 (2016).
- [26] V. G. Kogan and J. R. Kirtley, Meissner response of superconductors with inhomogeneous penetration depths, *Phys. Rev. B* **83**, 214521 (2011).
- [27] J. R. Cave and J. E. Evetts, Critical temperature profile determination using a modified london equation for inhomogeneous superconductors, *J. Low Temp. Phys.* **63**, 35 (1986).
- [28] E. H. Brandt, Thin superconductors and SQUIDs in perpendicular magnetic field, *Phys. Rev. B* **72**, 024529 (2005).
- [29] J. D. Jackson, Classical electrodynamics, 3rd ed., *Am. J. Phys.* **67**, 841 (1999).
- [30] L. Bishop-Van Horn and K. A. Moler, SuperScreen: An open-source package for simulating the magnetic response of two-dimensional superconducting devices, *Comput. Phys. Commun.* **280**, 108464 (2022).
- [31] M. Durkin, R. Garrido-Menacho, S. Gopalakrishnan, N. K. Jaggi, J.-H. Kwon, J.-M. Zuo, and N. Mason, Rare-region onset of superconductivity in niobium nanoislands, *Phys. Rev. B* **101**, 035409 (2020).
- [32] M. E. Huber, N. C. Koshnick, H. Bluhm, L. J. Archuleta, T. Azua, P. G. Björnsson, B. W. Gardner, S. T. Halloran, E. A. Lucero, and K. A. Moler, Gradiometric micro-SQUID susceptometer for scanning measurements of mesoscopic samples, *Rev. Sci. Instrum.* **79**, 053704 (2008).
- [33] J. Pearl, Current distribution in superconducting films carrying quantized fluxoids, *Appl. Phys. Lett.* **5**, 65 (1964).
- [34] J. R. Kirtley, B. Kalisky, J. A. Bert, C. Bell, M. Kim, Y. Hikita, H. Y. Hwang, J. H. Ngai, Y. Segal, F. J. Walker, C. H. Ahn, and K. A. Moler, Scanning SQUID susceptometry of a paramagnetic superconductor, *Phys. Rev. B* **85**, 224518 (2012).
- [35] P. Dubos, H. Courtois, B. Pannetier, F. K. Wilhelm, A. D. Zaikin, and G. Schon, Josephson critical current in a long mesoscopic S-N-S junction, *Phys. Rev. B* **63**, 064502 (2001).
- [36] L. D. R. Beal, D. C. Hill, R. A. Martin, and J. D. Hedengren, GEKKO optimization suite, *Processes* **6**, 106 (2018).
- [37] J. D. Hedengren, R. A. Shishavan, K. M. Powell, and T. F. Edgar, Nonlinear modeling, estimation and predictive control in APMonitor, *Comput. Chem. Eng.* **70**, 133 (2014).
- [38] P. G. de Gennes, Boundary effects in superconductors, *Rev. Mod. Phys.* **36**, 225 (1964).
- [39] C. J. Lobb, D. W. Abraham, and M. Tinkham, Theoretical interpretation of resistive transition data from arrays of superconducting weak links, *Phys. Rev. B* **27**, 150 (1983).
- [40] J. R. Phillips, H. S. J. van der Zant, J. White, and T. P. Orlando, Influence of induced magnetic fields on the static properties of Josephson-junction arrays, *Phys. Rev. B* **47**, 5219 (1993).
- [41] A. L. Fetter, Flux penetration in a thin superconducting disk, *Phys. Rev. B* **22**, 1200 (1980).
- [42] V. A. Schweigert and F. M. Peeters, Flux Penetration and Expulsion in Thin Superconducting Disks, *Phys. Rev. Lett.* **83**, 2409 (1999).
- [43] T. R. Lemberger and J. Draskovic, Theory of the lower critical magnetic field for a two-dimensional superconducting film in a nonuniform field, *Phys. Rev. B* **87**, 064503 (2013).
- [44] T. R. Lemberger and A. Ahmed, Upper limit of metastability of the vortex-free state of a two-dimensional superconductor in a nonuniform magnetic field, *Phys. Rev. B* **87**, 214505 (2013).
- [45] J. Draskovic, T. R. Lemberger, B. Peters, F. Yang, J. Ku, A. Bezryadin, and S. Wang, Measuring the superconducting coherence length in thin films using a two-coil experiment, *Phys. Rev. B* **88**, 134516 (2013).
- [46] M. Tinkham, *Introduction to Superconductivity*, 2nd ed. (Dover, Mineola, NY, 2004).
- [47] T. R. Lemberger and Y. L. Loh, Vortex dynamics in a thin superconducting film with a non-uniform magnetic field applied at its center with a small coil, *J. Appl. Phys.* **120**, 163904 (2016).
- [48] M. A. Galin, F. Rudau, E. A. Borodianskyi, V. V. Kurin, D. Koelle, R. Kleiner, V. M. Krasnov, and A. M. Klushin, Direct Visualization of Phase-Locking of Large Josephson Junction Arrays by Surface Electromagnetic Waves, *Phys. Rev. Applied* **14**, 024051 (2020).